

# Near-Field Localization and Phase Shift Optimization for RIS-Assisted Non-Ideal OFDM Systems

Hanfu Zhang, *Graduate Student Member, IEEE*, Erwu Liu, *Senior Member, IEEE*, Rui Wang, *Senior Member, IEEE*, Zhe Xing, *Graduate Student Member, IEEE*, and Yan Liu, *Member, IEEE*

**Abstract**—By incorporating *reconfigurable intelligent surface* (RIS) into communication-assisted localization systems, the issue of signal blockage caused by obstacles can be addressed, and passive beamforming can be employed to enhance localization accuracy. However, existing works mainly consider ideal channels and do not account for the effects of realistic impairments like *carrier frequency offset* (CFO) and *phase noise* (PN) on localization. This paper proposes an iterative joint estimation algorithm for CFO, PN, and user position based on *maximum a posteriori* (MAP) criterion and *gradient descent* (GD) algorithm. Closed-form expressions for CFO and PN updates are provided. The *hybrid Cramér-Rao lower bound* (HCRLB) for the estimation parameters is derived, and the ambiguity in CFO and PN estimation is analyzed. To minimize the HCRLB, a non-convex RIS shift optimization problem is formulated and is transformed into a convex *semidefinite programming* (SDP) problem using the technique of *semidefinite relaxation* (SDR) and Schur complement. After optimizing the RIS phase shift, the theoretical positioning accuracy within the *area of interest* (AOI) can be improved by two orders of magnitude, with a maximum positioning *root mean square error* (RMSE) lower than  $10^{-2}$  m.

**Index Terms**—Near-field localization, reconfigurable intelligent surface, passive beamforming, carrier frequency offset, phase noise.

## I. INTRODUCTION

WITH the widespread application of *fifth-generation* (5G) networks worldwide, research focus has shifted towards future *sixth generation* (6G) mobile communication technologies. For 5G mobile networks, the demand for positioning accuracy has already reached sub-meter levels due to the need to support various location-based services. In 6G networks, it is expected that high-precision positioning at the centimeter level will play an even more important role [1], [2], [3]. While *global navigation satellite systems* (GNSSs) have been widely used in various positioning scenarios [25], they suffer from issues such as insufficient positioning accuracy and signal instability due to obstacles [26], [27]. In recent years, research has been conducted on using communication signals to assist in positioning, aiming to achieve more accurate and

This work has been submitted to the IEEE for possible publication. Copyright may be transferred without notice, after which this version may no longer be accessible.

The authors are with the College of Electronic and Information Engineering, Tongji University, Shanghai 201804, China (e-mail: hanfuzhang@tongji.edu.cn; erwu.liu@ieee.org; ruiwang@tongji.edu.cn; zxing@tongji.edu.cn; yanliu2022@tongji.edu.cn). The authors would like to thank the colleagues at the Sino-German Center of Intelligent Systems, Tongji University.

continuous positioning alongside GNSS signals. For example, Shahmansoori *et al.* [10] proposed a three-stage positioning algorithm that improves the *simultaneous orthogonal matching pursuit* (SOMP) algorithm and the *space alternating generalized expectation-maximization* (SAGE) algorithm, and exploited the sparsity of millimeter-wave *multiple-input multiple-output* (MIMO) channels to lower the complexity of the channel model. Hu *et al.* [11] presented a *two-dimensional* (2D) positioning algorithm based on the *estimating signal parameters via rotational invariance technique* (ESPRIT), which estimates user positions by constructing signal subspaces. The estimator has closed-form expressions, which reduces the computational complexity significantly compared to traditional estimation methods. However, in these methods that utilize communication signals for localization, the problem of signal blockage by obstacles still remains unavoidable.

In recent years, *reconfigurable intelligent surface* (RIS) technology has emerged as a key enabling technology for 6G networks [4], [5], [23]. This technology allows for reconfiguring wireless channel environments, enabling communication even when the *line-of-sight* (LoS) link is obstructed. Introducing the RIS to assist in communication-based positioning has become a research focus [32], [31]. From the perspective of mobility, the research can be divided into two categories: static positioning [17], [18], [19] and dynamic positioning [15], [13]. The former considers scenarios where the user undergoes minimal movement within a coherent time, and the latter involves scenarios with the opposite characteristic. From the perspective of positioning distance, the research can also be divided into two categories: far-field positioning [19], [13], [20] and near-field positioning [18], [19], [13], [24]. In the far-field case, the distance between the user and the RIS exceeds Fraunhofer distance [8], and the signal can be approximated as a planar wave. Conversely, in the near-field case, the signal cannot be treated as parallel propagation and should be considered a spherical wave.

For example, Luan *et al.* [12] focused on the near-field static 2D positioning scenario. The authors proposed a robust optimization method to optimize the RIS phase shift for improving localization accuracy. The paper also investigated the power optimization problem of the localization system. Elzanaty *et al.* [13] studied RIS-assisted localization for multi-antenna mobile users. They proposed a *three-dimensional* (3D) model that can be applied in both far-field and near-field scenarios and analyzed the position and orientation error

bounds. Lin *et al.* [14] introduced a novel twin-RIS configuration comprising two RISs with relative spatial rotation. To extract the parameters of the cascaded channel, the authors employed array signal processing and atomic norm denoising techniques. They established nonlinear equations based on the characteristics of the twin-RIS structure and accurately recovered the multipath parameters. User localization for static users in the far-field scenario is then performed based on the estimated channel parameters. Teng *et al.* [15] introduced a new message-passing algorithm called BULT to effectively solve the localization problem for mobile users in the far-field scenario. They also derived the Bayesian Cramér-Rao lower bound for the proposed algorithm.

Although there has been extensive research on user localization with RIS in various scenarios such as static, dynamic, far-field, and near-field, most of the existing works assumed ideal channel conditions without considering realistic impairments like *carrier frequency offset* (CFO) and *phase noise* (PN) that can introduce uncertainties and affect system performance. Only a few studies have considered modeling certain interferences. For example, [13], [20], [16] took into account clock offset, and [16] considered phase offset. However, to the best of our knowledge, there is currently no research that specifically analyzed CFO and PN in RIS-assisted *orthogonal frequency division multiplexing* (OFDM) localization systems.

In an OFDM system, CFO and PN can convolve with the data symbols, causing signal constellation rotation and introducing *inter-carrier interference* (ICI). This interference significantly degrades the overall system performance. Moreover, most aforementioned works have assumed the subcarriers' signals are independent, which cannot hold in the presence of CFO and PN due to the absence of ICI. Therefore, localization algorithms need to leverage the received time-domain signals to account for these effects and accurately estimate the user's position in this case.

In this paper, we consider the problem of joint estimation of CFO, PN, and user position in a RIS-assisted OFDM system. The contributions of this paper are outlined as follows.

- We investigate the problem of static near-field localization in an OFDM system assisted by RIS, considering the effects of CFO and PN. Moreover, we establish a time-domain model and introduce the frequency-domain channel with time-delay parameters into the model through time-frequency transformation to meet the requirements of position estimation.
- We propose an iterative estimation approach based on the *maximum a posteriori* (MAP) criterion and *gradient descent* (GD) algorithm to jointly estimate the CFO, the PN, and the user position. The algorithm significantly reduces complexity by deriving closed-form expressions for CFO and PN estimation.
- We derive the *hybrid Cramér-Rao lower bound* (HCRLB) for the joint estimation problem and analyze the phase ambiguity issue in CFO and PN estimation. A new metric is introduced to evaluate the accuracy of joint CFO and PN estimation.
- We implement phase shift optimization for RIS to enhance the theoretical positioning accuracy. By applying

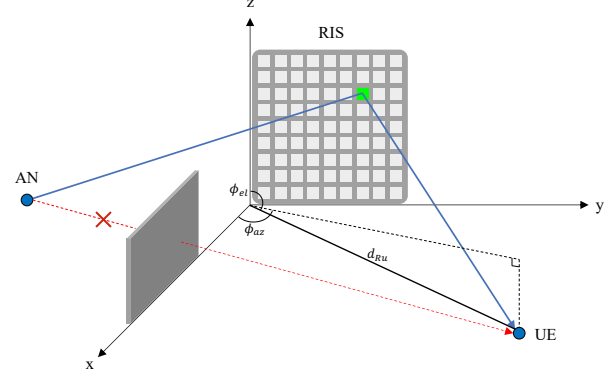


Fig. 1. RIS-aided 3D localization scenario, where the LoS link is blocked.

the *semidefinite relaxation* (SDR) method and utilizing the Schur complement, we convert the initially non-convex optimization problem into a convex *semidefinite programming* (SDP) problem. It is shown that the theoretical positioning accuracy has been improved by two orders of magnitude.

The paper is structured as follows. Section II introduces the system model, while Section III presents the joint estimation algorithm. Section IV is dedicated to the derivation of the HCRLB for the proposed joint estimation problem. The proposed RIS phase shift optimization method is discussed in Section V. Section VI showcases comprehensive simulation results, and the paper concludes in Section VII.

*Notations:*  $\mathbb{E}(\cdot)$ ,  $p(\cdot)$  denote the expectation and the *probability density function* (PDF) of the argument, respectively.  $\text{tr}(\mathbf{M})$ ,  $\det \mathbf{M}$ ,  $\mathbf{M}^\top$ ,  $\mathbf{M}^*$ ,  $\mathbf{M}^H$ ,  $\mathbf{M}^{-1}$  denote the trace, determinant, transpose, conjugate, hermitian, and inverse of matrix  $\mathbf{M}$ , respectively.  $\text{Diag}(\mathbf{v})$  indicates a diagonal matrix created by assigning the elements of vector  $\mathbf{v}$  along its main diagonal.  $\mathbf{v}[n]$  denotes the  $n$ -th entry of vector  $\mathbf{v}$ . Unless otherwise specified, all indices in the article start from 0.  $\text{Blkdiag}(\mathbf{M}_0, \mathbf{M}_1, \dots, \mathbf{M}_{N-1})$  denotes a block diagonal matrix with  $\mathbf{M}_0, \mathbf{M}_1, \dots, \mathbf{M}_{N-1}$  being its diagonal matrices.  $[\mathbf{M}]_{i:j,:}$  refers to a submatrix encompassing rows  $i$  to  $j$  and all columns of matrix  $\mathbf{M}$ , while  $[\mathbf{M}]_{:,i:j}$  denotes a submatrix encompassing columns  $i$  to  $j$  and all rows of matrix  $\mathbf{M}$ .  $\mathbf{0}_{M \times N}$ , and  $\mathbf{I}_M$  denote  $M \times N$  zeros matrix, and  $M \times M$  identity matrix, respectively.  $\Re\{\cdot\}$  and  $\Im\{\cdot\}$  represent the real and imaginary components of the complex value, respectively.  $\mathbb{C}^{m \times n}$  and  $\mathbb{R}^{m \times n}$  denote  $m \times n$  matrices with complex and real entries, respectively. Finally,  $\mathcal{CN}(\mu, \Sigma)$  and  $\mathcal{N}(\mu, \Sigma)$  represent complex and real Gaussian distributions, respectively, characterized by a mean vector  $\mu$  and covariance matrix  $\Sigma$ .

## II. SYSTEM MODEL

Fig. 1 illustrates the RIS-assisted OFDM downlink wireless communication system under consideration, comprising a single *anchor node* (AN) and a single *user equipment* (UE). In this scenario, we make the assumption that there are obstacles blocking the LoS path between AN and UE, and the *channel state information* (CSI) remains unchanged during the localization process, i.e., within the duration of one OFDM

symbol, similar to [19], [12], [16]. The positions of the AN and each element of the RIS are assumed to be known, which can be denoted as  $\mathbf{p}_a$ , and  $\mathbf{p}_r = [x_r, y_r, z_r]^\top$ , respectively, where  $r$  represents the index of the RIS element among a total of  $N_R$  elements. The position of UE, which is the primary parameter to be estimated, is denoted as  $\mathbf{p}_u = [x_u, y_u, z_u]^\top$ .

The RIS elements are organized in the form of a *uniform planar array* (UPA). We take the bottom-left corner of the RIS as the reference point and place it at the coordinate origin. The RIS is positioned on the  $yz$  plane, and both edges on the coordinate axes are located in the positive half-axis. The coordinates of the  $r$ -th RIS element can be represented as  $\mathbf{p}_r = [0, d \times ((r-1) \bmod N_R), d \times \lceil \frac{r}{\sqrt{N_R}} - 1 \rceil]^\top$ , where  $d$  stands for the element spacing of RIS, whose value is typically set as half of the wavelength. To satisfy the conditions of the near-field setup, both the distance between AN and RIS, as well as the distance between RIS and UE, should lie within the Fresnel region [8]. Specifically, the distances should lie within the interval  $[0.62\sqrt{D^3/\lambda}, 2D^2/\lambda]$ , where  $D = \sqrt{2}d(\sqrt{N_R} - 1)$  represents the aperture of RIS and  $\lambda$  is the operating wavelength. Additionally, we adopt a polar coordinate system for estimating the user's position, i.e., using  $d_{Ru}$ ,  $\phi_{az}$ ,  $\phi_{el}$  to express the user's position, which represents the distance, azimuth angle, and elevation angle of UE relative to the coordinate origin, respectively. The transformation relationships between these three parameters and  $x_u$ ,  $y_u$ ,  $z_u$  are as follows

$$d_{Ru} = \sqrt{x_u^2 + y_u^2 + z_u^2}, \quad (1a)$$

$$\phi_{az} = \arctan \frac{y_u}{x_u}, \quad (1b)$$

$$\phi_{el} = \arccos \frac{z_u}{\sqrt{x_u^2 + y_u^2 + z_u^2}}, \quad (1c)$$

and in turn, can be expressed as

$$x_u = d_{Ru} \sin \phi_{el} \cos \phi_{az}, \quad (2a)$$

$$y_u = d_{Ru} \sin \phi_{el} \sin \phi_{az}, \quad (2b)$$

$$z_u = d_{Ru} \cos \phi_{el}. \quad (2c)$$

The localization process in the paper is performed using one OFDM symbol, with  $N$  subcarriers, a center carrier frequency of  $f_c$ , corresponding to a wavelength of  $\lambda$ , and a signal bandwidth of  $B$ . Upon sampling at a rate of  $T_s = \frac{1}{NB}$  and removing the *cyclic prefix* (CP) at UE, the received time-domain signal can be represented as

$$\mathbf{y} = \sqrt{P} \Lambda_\phi \Lambda_\theta \mathbf{S}^\top \tilde{\mathbf{h}} + \tilde{\mathbf{v}}, \quad (3)$$

where

- $\mathbf{y} \triangleq [y[0], y[1], \dots, y[N-1]]^\top$ ,
- $P$  is the transmit power,
- $\Lambda_\phi$  is the impact caused by CFO on the signal. It is a diagonal matrix, and each item on the diagonal can be expressed as  $[\Lambda_\phi]_{n,n} = e^{j2\pi \frac{n\Delta f}{NB}} = e^{j2\pi \frac{n}{N}\phi}$ , where  $\phi = \frac{\Delta f}{B}$  is called the normalized CFO,
- $\Lambda_\theta \triangleq \text{Diag}[e^{j\theta[0]}, e^{j\theta[1]}, \dots, e^{j\theta[N-1]}]$  is the impact caused by PN on the signal, further details about which will be discussed in the later part of this section,

- $\mathbf{S} \triangleq \sqrt{N} \mathbf{F}^\text{H} \text{Diag}(\mathbf{s})$ , where  $\mathbf{F}^\text{H}$  is the *inverse fast Fourier transform* (IFFT) matrix and  $\mathbf{s}$  is the frequency domain transmitted symbol sequence at the AN,
- $\tilde{\mathbf{h}} \triangleq \mathbf{h}_{LoS} + \mathbf{h}_{NLoS}$  is the frequency domain channel, with  $\mathbf{h}_{LoS}$  and  $\mathbf{h}_{NLoS}$  representing the LoS and the *non-line-of-sight* (NLoS) part of the channel, respectively. We assume  $\mathbf{h}_{NLoS}$  follows a known distribution  $\mathbf{h}_{NLoS} \sim \mathcal{CN}(0, \sigma_{NLoS}^2 \mathbf{I}_N)$ . Hence, The impact caused by  $\mathbf{h}_{NLoS}$  on the signal can be combined with the additive Gaussian noise  $\tilde{\mathbf{v}}$ . Consequently, we can rewrite (3) as

$$\mathbf{y} = \sqrt{P} \Lambda_\phi \Lambda_\theta \mathbf{S}^\top \mathbf{h} + \mathbf{v}, \quad (4)$$

where  $\mathbf{h}$  and  $\mathbf{v}$  represent the LoS part of the channel and the combined noise, respectively.  $\mathbf{h}$  contains the known part of the channel from AN to RIS and the unknown part of the channel from RIS to UE. Each item of it can be expressed by  $\mathbf{h}[n] = \sum_{r=1}^{N_R} \sqrt{\rho_{aR,n,r}} \sqrt{\rho_{Ru,n,r}} \mathbf{w}[r] e^{-j2\pi \frac{nB}{N}(\tau_{ar} + \tau_{ru})}$ , where  $\sqrt{\rho_{aR,n,r}} = \frac{\sqrt{G_a} \lambda_n}{4\pi d_{ar}}$  and  $\sqrt{\rho_{Ru,n,r}} = \frac{\sqrt{G_t} \lambda_n}{4\pi d_{ru}}$  are the free-space path loss from AN to RIS, and from RIS to UE, respectively.  $\mathbf{w}[r]$  is the phase shift of the  $r$ -th element of RIS,  $\tau_{ar} = \frac{d_{ar}}{c} = \frac{\|\mathbf{p}_r - \mathbf{p}_a\|}{c}$  represents the delay from AN to the  $r$ -th element of RIS, while  $\tau_{ru} = \frac{d_{ru}}{c} = \frac{\|\mathbf{p}_u - \mathbf{p}_r\|}{c}$  denotes the delay from the  $r$ -th element of RIS to UE, with  $c$  representing the light speed,

- $\mathbf{v} \triangleq [v[0], v[1], \dots, v[N-1]]$  is the combined additive noise at UE, and follows the distribution  $\mathbf{v} \sim \mathcal{CN}(\mathbf{0}_{N \times 1}, \sigma^2 \mathbf{I}_N)$ .

Drawing upon the attributes of PN observed in practical oscillators, it can be effectively modeled as a Wiener process [22], i.e.,

$$\boldsymbol{\theta}[n] = \boldsymbol{\theta}[n-1] + \boldsymbol{\Delta}[n], \quad (5)$$

where  $\boldsymbol{\Delta}[n]$  is a real Gaussian variable with a distribution of  $\boldsymbol{\Delta}[n] \sim \mathcal{N}(0, \sigma_\Delta^2)$ . As in [21], it is assumed that  $\boldsymbol{\theta}[-1] = 0$ , and then we can obtain that the PN vector  $\boldsymbol{\theta} \triangleq [\theta[0], \theta[1], \dots, \theta[N-1]]^\top$  follows a distribution of  $\boldsymbol{\theta} \sim \mathcal{N}(\mathbf{0}_{N \times 1}, \boldsymbol{\Psi})$ , where  $\boldsymbol{\Psi}$  can be expressed by

$$\boldsymbol{\Psi} = \sigma_\Delta^2 \begin{bmatrix} 1 & 1 & 1 & \cdots & 1 & 1 \\ 1 & 2 & 2 & \cdots & 2 & 2 \\ 1 & 2 & 3 & 3 & \cdots & 3 \\ \vdots & \vdots & \vdots & \vdots & \ddots & \vdots \\ 1 & 2 & 3 & \cdots & N-1 & N \end{bmatrix}. \quad (6)$$

### III. PROPOSED JOINT POSITION, CFO AND PN ESTIMATION

In previous works [12], [16], localization was based on frequency-domain signals. However, in our problem, the introduction of CFO and PN would result in ICI if the signal is transformed into the frequency domain, which will increase the difficulty of our estimation. Therefore, in this paper, we conduct the estimation in the time domain. In this section, we propose an iterative algorithm based on MAP criterion and GD algorithm, which jointly estimates the normalized CFO, PN, and position of UE.

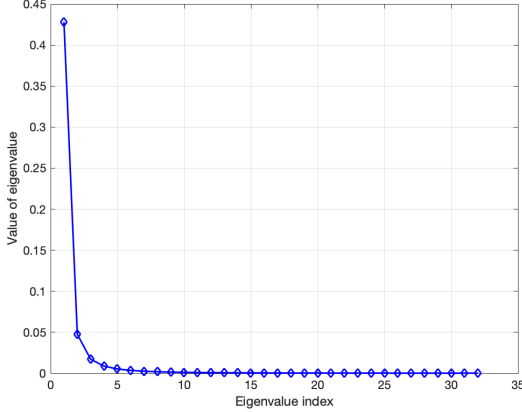


Fig. 2. Eigenvalues of  $\Psi$  at  $N = 32$  and  $\sigma_{\Delta}^2 = 10^{-3}$ .

By defining parameter vector  $\lambda \triangleq [\phi, \theta^T, d_{Ru}, \phi_{az}, \phi_{el}]^T$ , whereas  $\theta$  is a random variable, and the others are deterministic variables, the posterior distribution of  $\lambda$  given the received signal  $\mathbf{y}$  can be written as

$$p(\lambda | \mathbf{y}) = \frac{p(\mathbf{y} | \lambda) \times p(\theta)}{p(\mathbf{y})}. \quad (7)$$

After removing the constant terms, the object function can be expressed as  $\mathcal{L}(\lambda) = -\log p(\mathbf{y} | \lambda) - \log p(\theta)$ , and our goal is to achieve the joint estimation of  $\lambda$  by optimizing the following unconstrained function.

$$\hat{\lambda} \propto \arg \min_{\lambda} \mathcal{L}(\lambda). \quad (8)$$

#### A. Phase Noise Estimation

1) *Approximation of PN vector:* From (4), it can be observed that there are multiple parameters that need to be jointly estimated. In order to alleviate the computational complexity at UE, we take advantage of the properties of the PN vector to approximate it. This approach results in a reduction of unknown parameters that require estimation. As depicted in Fig. 2, the eigenvalues of  $\Psi$  mostly cluster around zero. This observation allows us to approximate the PN vector as follows

$$\theta \approx \Pi \eta, \quad (9)$$

where  $\eta \sim \mathcal{N}(\mathbf{0}_{L \times 1}, \mathbf{I}_L)$  contains  $L \leq N$  PN parameters, and  $\Pi \in \mathbb{R}^{N \times L}$  is the transformation matrix. To derive  $\Pi$ , we first perform *singular value decomposition* (SVD) on  $\Psi$ , which is given by  $\Psi = \mathbf{U} \mathbf{D} \mathbf{U}^T$ , where  $\mathbf{D} = \text{Diag}(e)$ , and  $e$  represents the eigenvalues of  $\Psi$  arranged in descending order. Subsequently,  $\Pi$  can be calculated by  $\Pi = [\mathbf{U}]_{:, 0:L-1} \times \sqrt{e}$ . In the subsequent analysis,  $\eta$  is estimated instead of  $\theta$ .

2) *Estimation of approximate PN vector:* After approximating the PN parameter  $\theta$ , the objective function can be rewritten as

$$\begin{aligned} \mathcal{L}(\lambda) &= -\log p(\mathbf{y} | \lambda) - \log p(\eta) \\ &\propto \frac{1}{\sigma^2} \|\mathbf{y} - \mu\|^2 + \frac{1}{2} \eta^T \eta, \end{aligned} \quad (10)$$

where  $\mu \triangleq \sqrt{P} \Lambda_{\phi} \Lambda_{\theta} \mathbf{S}^T \mathbf{h}$  is the received signal at UE without additive noise, and the noise variance  $\sigma^2$  is assumed to be known.

Due to the typically small PN variance in practical oscillators, the elements of  $\Lambda_{\theta}$  can be approximated by employing a first-order Taylor series expansion, resulting in  $e^{j\theta[n]} \approx 1 + j\theta[n]$ . Consequently, we can approximate  $\Lambda_{\theta}$  as  $\Lambda_{\theta} \approx \mathbf{I}_N + j\text{Diag}(\Pi \eta)$ . With this approximation, the objective function in (10) can be reformulated as:

$$\begin{aligned} \mathcal{L}_{\eta}^{[q+1]} &\approx \frac{1}{\sigma^2} (\bar{\mathbf{y}} - \mathbf{Q} \eta)^H (\bar{\mathbf{y}} - \mathbf{Q} \eta) + \frac{1}{2} \eta^T \eta \\ &= \frac{1}{\sigma^2} (\bar{\mathbf{y}}^H \bar{\mathbf{y}} - 2\Re \{ \bar{\mathbf{y}}^H \mathbf{Q} \} \eta + \eta^T \Re \{ \mathbf{Q}^H \mathbf{Q} \} \eta) \\ &\quad + \frac{1}{2} \eta^T \eta, \end{aligned} \quad (11)$$

where  $\bar{\mathbf{y}} \triangleq \mathbf{y} - \sqrt{P} \hat{\Lambda}_{\phi}^{[q]} \mathbf{S}^T \hat{\mathbf{h}}^{[q]}$ , and  $\mathbf{Q} \triangleq j\sqrt{P} \text{Diag}(\hat{\Lambda}_{\phi}^{[q]} \mathbf{S}^T \hat{\mathbf{h}}^{[q]}) \Pi$ . The superscript  $q$  represents the round number of iterations.

Subsequently, by setting the gradient of (11) equal to zero, i.e.,

$$\frac{\partial \mathcal{L}_{\eta}^{[q+1]}}{\partial \eta} = -\frac{2}{\sigma^2} \Re \{ \mathbf{Q}^H \bar{\mathbf{y}} \} + \frac{2}{\sigma^2} \Re \{ \mathbf{Q}^H \mathbf{Q} \} \eta + \eta = \mathbf{0}_{L \times 1}, \quad (12)$$

we obtain

$$\hat{\eta}^{[q+1]} = \left[ \Re \{ \mathbf{Q}^H \mathbf{Q} \} + \frac{1}{2} \sigma^2 \mathbf{I}_L \right]^{-1} \Re \{ \mathbf{Q}^H \bar{\mathbf{y}} \}. \quad (13)$$

#### B. CFO Estimation

To estimate the CFO, we solve the following unconstrained problem

$$\hat{\phi} \propto \arg \min_{\phi} \mathcal{L}_{\phi} \propto \arg \min_{\phi} \|\mathbf{y} - \mu\|^2. \quad (14)$$

In order to enhance the tractability of the problem presented in (14) and obtain a closed-form solution, we employ a Taylor series approximation once more. The  $n$ -th term on the diagonal of  $\Lambda_{\phi}$  can be approximated as

$$[\Lambda_{\phi}]_{n,n} = e^{j2\pi \frac{n}{N} \phi} \approx e^{j2\pi \frac{n}{N} \hat{\phi}} + (\phi - \hat{\phi}) \frac{j2\pi}{N} e^{j2\pi \frac{n}{N} \hat{\phi}}. \quad (15)$$

Hence,  $\hat{\Lambda}_{\phi}^{[q+1]}$  can be approximated as

$$\hat{\Lambda}_{\phi}^{[q+1]} \approx \hat{\Lambda}_{\phi}^{[q]} + (\phi - \hat{\phi}^{[q]}) \tilde{\Lambda}_{\phi}^{[q]}, \quad (16)$$

where  $[\tilde{\Lambda}_{\phi}^{[q]}]_{n,n} = \frac{j2\pi n}{N} e^{j2\pi n \hat{\phi}^{[q]}}$ .

With (16),  $\mathcal{L}_{\phi}$  in (14) can be rewritten as

$$\mathcal{L}_{\phi}^{[q+1]} \approx \frac{1}{\sigma^2} \|\mathbf{y} - [\hat{\Lambda}_{\phi}^{[q]} + (\phi - \hat{\phi}^{[q]}) \tilde{\Lambda}_{\phi}^{[q]}] \mathbf{d}\|^2, \quad (17)$$

where  $\mathbf{d} \triangleq \sqrt{P} \hat{\Lambda}_{\theta}^{[q+1]} \mathbf{S}^T \hat{\mathbf{h}}^{[q]}$ . Upon setting the gradient of (17) equal to zero, and solving for  $\phi$ , we can obtain the closed-form expression of  $\hat{\phi}$  at the  $(q+1)$ -th iteration as

$$\hat{\phi}^{[q+1]} = \hat{\phi}^{[q]} + \frac{\Re \left\{ (\mathbf{y} - \hat{\Lambda}_{\phi}^{[q]} \mathbf{d})^H \tilde{\Lambda}_{\phi}^{[q]} \mathbf{d} \right\}}{\mathbf{d}^H \tilde{\Lambda}_{\phi}^{[q]} \mathbf{d}}. \quad (18)$$

### C. Position Estimation

For position estimation, we employ the GD algorithm. Due to the similarity in the derivative expressions of the objective function with respect to three positional parameters  $d_{Ru}$ ,  $\phi_{az}$ , and  $\phi_{el}$ , we use the symbol  $\xi$  to represent any one of them. The expression for the partial derivative of the objective function with respect to  $\xi$  is as follows

$$\frac{\partial \mathcal{L}_\xi}{\partial \xi} = \frac{2}{\sigma^2} \Re \left\{ \left( \mathbf{P} \mathbf{h}^H \mathbf{S}^* \mathbf{S}^\top - \sqrt{P} \mathbf{y}^H \boldsymbol{\Lambda}_\theta \boldsymbol{\Lambda}_\phi \mathbf{S}^\top \right) \frac{\partial \mathbf{h}}{\partial \xi} \right\}, \quad (19)$$

where each term of  $\frac{\partial \mathbf{h}}{\partial \xi}$  can be calculated as follows

$$\begin{aligned} \frac{\partial \mathbf{h}}{\partial \xi}[n] &= \frac{\partial \mathbf{h}[n]}{\partial \xi} = - \sum_{r=1}^{N_R} \sqrt{\rho_{aR,n,r}} \sqrt{\rho_{Ru,n,r}} \mathbf{w}[r] \\ &\times e^{-j2\pi \frac{nB}{N}(\tau_{ar} + \tau_{ru})} \left( \frac{1}{d_{ru}} + j2\pi \frac{nB}{Nc} \right) \frac{\partial d_{ru}}{\partial \xi}, \end{aligned} \quad (20)$$

with  $\frac{\partial d_{ru}}{\partial \xi}$ ,  $\xi = d_{Ru}, \phi_{az}, \phi_{el}$ , being

$$\begin{aligned} \frac{\partial d_{ru}}{\partial d_{Ru}} &= \frac{1}{d_{Ru}} [(d_{Ru} \sin \phi_{el} \cos \phi_{az} - x_r) \sin \phi_{el} \cos \phi_{az} \\ &+ (d_{Ru} \sin \phi_{el} \sin \phi_{az} - y_r) \sin \phi_{el} \sin \phi_{az} \\ &+ (d_{Ru} \cos \phi_{el} - z_r) \cos \phi_{el}], \end{aligned} \quad (21)$$

$$\begin{aligned} \frac{\partial d_{ru}}{\partial \phi_{az}} &= \frac{1}{d_{Ru}} [(d_{Ru} \sin \phi_{el} \cos \phi_{az} - x_r) (-\sin \phi_{az} d_{Ru} \sin \phi_{el}) \\ &+ (d_{Ru} \sin \phi_{el} \sin \phi_{az} - y_r) d_{Ru} \sin \phi_{el} \cos \phi_{az}], \end{aligned} \quad (22)$$

and

$$\begin{aligned} \frac{\partial d_{ru}}{\partial \phi_{el}} &= \frac{1}{d_{Ru}} [(d_{Ru} \sin \phi_{el} \cos \phi_{az} - x_r) d_{Ru} \cos \phi_{az} \cos \phi_{el} \\ &+ (d_{Ru} \sin \phi_{el} \sin \phi_{az} - y_r) d_{Ru} \sin \phi_{az} \cos \phi_{el} \\ &+ (d_{Ru} \cos \phi_{el} - z_r) (-d_{Ru} \sin \phi_{el})]. \end{aligned} \quad (23)$$

The general iterative joint estimation algorithm is outlined in Algorithm 1.

### D. Estimation Performance Evaluation

For position estimation, we use *root mean square error* (RMSE) as the performance metric. For any testing UE position  $\mathbf{p}_u$ , RMSE<sub>u</sub> can be expressed as

$$\text{RMSE}_u = \sqrt{\frac{1}{M_e} \sum_{m=1}^{M_e} \|\hat{\mathbf{p}}_{u,m} - \mathbf{p}_u\|^2}, \quad (24)$$

where  $M_e$  is the Monte Carlo experiment amount, and  $\hat{\mathbf{p}}_{u,m}$  represents the estimation of UE position in the  $m$ -th trial.

For CFO and PN estimation, it can be straightforwardly observed from (4) that, the received signal  $\mathbf{y}$  is not altered under a common phase rotation  $\epsilon$ , i.e.,

$$\hat{\phi} \rightarrow \phi - \epsilon, \hat{\theta} \rightarrow \theta + \epsilon, \quad (25)$$

where  $\epsilon[n] = \frac{2\pi n \epsilon}{N}$ . Equation (25) indicates that there exists ambiguity in estimating CFO and PN. The ambiguity leads to difficulties in achieving high estimation accuracy for individual parameters of CFO and PN. However, in this paper, we are

---

### Algorithm 1 Iterative joint estimation algorithm.

- 1: Optimize RIS phase shift  $\mathbf{w}$  using the method to be introduced in Section V.
- 2: Initialize estimation of normalized CFO  $\hat{\phi}$  and UE position  $\hat{\mathbf{p}}_u$ , step length  $k_p$ , convergence accuracy for outer loop  $\epsilon_o$ , convergence accuracy for inner loop  $\epsilon_i$ , and calculate corresponding polar coordinate of  $\hat{\mathbf{p}}_u$  using (1).
- 3: **repeat**
- 4:   Update  $\hat{\eta}$  with  $\hat{\phi}, \hat{\mathbf{p}}_u$  being fixed using (13);
- 5:   Update  $\hat{\theta}$  using (9);
- 6:   Update  $\hat{\phi}$  with  $\hat{\theta}, \hat{\mathbf{p}}_u$  being fixed using (18);
- 7: **repeat**
- 8:    $\hat{d}_{Ru} \leftarrow \hat{d}_{Ru} - \frac{\partial \mathcal{L}_\xi}{\partial d_{Ru}} k_p$ ;
- 9:    $\hat{\phi}_{az} \leftarrow \hat{\phi}_{az} - \frac{\partial \mathcal{L}_\xi}{\partial \phi_{az}} k_p$ ;
- 10:    $\hat{\phi}_{el} \leftarrow \hat{\phi}_{el} - \frac{\partial \mathcal{L}_\xi}{\partial \phi_{el}} k_p$ ;
- 11: **until**  $\mathcal{L}^{[p]} - \mathcal{L}^{[p+1]} \leq \epsilon_i$  after the  $p$ -th iteration.
- 12: **until**  $\mathcal{L}^{[q]} - \mathcal{L}^{[q+1]} \leq \epsilon_o$  after the  $q$ -th iteration.  $\epsilon_i$  and  $\epsilon_o$  are both pre-set convergence accuracy and should vary with changes in transmit power.
- 13: Calculate Cartesian coordinate of  $\hat{\mathbf{p}}_u$  using (2).

---

not focusing on the separate estimation accuracy of CFO and PN but rather on the estimation accuracy of UE position. Therefore, it is acceptable as long as the overall estimation accuracy of CFO and PN is reduced. In this paper, to evaluate the overall estimation accuracy of CFO and PN, we utilize a novel joint *mean square error* (MSE) measure, which can be calculated as

$$\text{MSE}_{\phi, \theta} = \mathbb{E}_{\phi, \theta} (\|\underline{\gamma} - \hat{\gamma}\|^2), \quad (26)$$

where  $\underline{\gamma} = \gamma - \gamma[0]\mathbf{1}$ ,  $\hat{\gamma} = \hat{\gamma} - \hat{\gamma}[0]\mathbf{1}$ ,  $\gamma = [\gamma[0], \gamma[1], \dots, \gamma[N-1]]^\top$ ,  $\gamma[n] = \theta[n] + \frac{2\pi n \phi}{N}$ ,  $\hat{\gamma} = [\hat{\gamma}[0], \hat{\gamma}[1], \dots, \hat{\gamma}[N-1]]^\top$ ,  $\hat{\gamma}[n] = \hat{\theta}[n] + \frac{2\pi n \hat{\phi}}{N}$ .

### IV. HYBRID CRAMÉR-RAO LOWER BOUND ANALYSIS

In this section, we derive HCRLB to evaluate the joint estimation, in the presence of a random parameter  $\theta$  in the set of parameters to be estimated. The HCRLB for  $\lambda$ , the parameters to be estimated, is given by [7]

$$\mathbb{E}_{\mathbf{y}, \theta | \phi, d_{Ru}, \phi_{az}, \phi_{el}} [(\lambda - \hat{\lambda})(\lambda - \hat{\lambda})^\top] \succeq \mathbf{B}^{-1}, \quad (27)$$

where  $\mathbf{B}$  is the *Bayesian information matrix* (BIM), which can be calculated as

$$\mathbf{B} = \mathbb{E}_\theta [\mathbf{FIM}(\mathbf{y}; \lambda)] + \mathbb{E}_\theta \left[ -\frac{\partial}{\partial \lambda} \left( \frac{\partial \log p(\theta)}{\partial \lambda} \right)^\top \right]. \quad (28)$$

In order to evaluate the positioning accuracy and the CFO-PN joint MSE, we define a new parameter vector  $\alpha = \mathbf{g}(\lambda) \triangleq [\gamma, x_u, y_u, z_u]^\top$ . In the following subsections, we first derive the expression for matrix  $\mathbf{B}$ . Then, we derive the transition matrix to transform  $\mathbf{B}$  into the HCRLB relative to the parameter vector  $\alpha$ .

### A. Derivation of $\mathbb{E}_{\boldsymbol{\theta}}[\mathbf{FIM}(\mathbf{y}; \boldsymbol{\lambda})]$

To derive  $\mathbb{E}_{\boldsymbol{\theta}}[\mathbf{FIM}(\mathbf{y}; \boldsymbol{\lambda})]$ , we begin by calculating the *Fisher information matrix* (FIM) for  $\boldsymbol{\lambda}$ , as expressed by

$$[\mathbf{FIM}(\mathbf{y}; \boldsymbol{\lambda})]_{i,j} = \frac{2}{\sigma^2} \Re \left\{ \frac{\partial \boldsymbol{\mu}^H}{\partial \lambda_i} \frac{\partial \boldsymbol{\mu}}{\partial \lambda_j} \right\}. \quad (29)$$

To calculate (29), the following gives the derivative of  $\boldsymbol{\mu}$  with respect to each element in vector  $\boldsymbol{\lambda}$ .

$$\frac{\partial \boldsymbol{\mu}}{\partial \phi} = \sqrt{P} \boldsymbol{\Lambda} \boldsymbol{\Lambda}_\phi \boldsymbol{\Lambda}_\theta \mathbf{S}^\top \mathbf{h}, \quad (30a)$$

$$\frac{\partial \boldsymbol{\mu}}{\partial \boldsymbol{\theta}[n]} = \sqrt{P} \text{Diag}(\mathbf{a}[n]) \boldsymbol{\Lambda}_\phi \mathbf{S}^\top \mathbf{h}, \quad (30b)$$

$$\frac{\partial \boldsymbol{\mu}}{\partial d_{Ru}} = \sqrt{P} \boldsymbol{\Lambda} \boldsymbol{\Lambda}_\theta \mathbf{S}^\top \frac{\partial \mathbf{h}}{\partial d_{Ru}}, \quad (30c)$$

$$\frac{\partial \boldsymbol{\mu}}{\partial \phi_{az}} = \sqrt{P} \boldsymbol{\Lambda} \boldsymbol{\Lambda}_\theta \mathbf{S}^\top \frac{\partial \mathbf{h}}{\partial \phi_{az}}, \quad (30d)$$

$$\frac{\partial \boldsymbol{\mu}}{\partial \phi_{el}} = \sqrt{P} \boldsymbol{\Lambda}_\phi \boldsymbol{\Lambda}_\theta \mathbf{S}^\top \frac{\partial \mathbf{h}}{\partial \phi_{el}}, \quad (30e)$$

where  $\boldsymbol{\Lambda}$  is a diagonal matrix,  $[\boldsymbol{\Lambda}]_{n,n} = \frac{j2\pi n}{N}$ ,  $\mathbf{a}[n] = [\mathbf{0}_{1 \times n}, j e^{j\theta[n]}, \mathbf{0}_{1 \times (N-n-1)}]^\top$ .

It is not difficult to observe that in (30), the terms related to  $\phi$  and  $\boldsymbol{\theta}$  all appear in the exponential terms of the diagonal elements of the corresponding matrix. Hence, they would disappear when calculating  $\frac{\partial \boldsymbol{\mu}^H}{\partial \lambda_i} \frac{\partial \boldsymbol{\mu}}{\partial \lambda_j}$  in (29). That is to say, the calculated FIM is not related to parameter  $\theta$ , and

$$\mathbb{E}_{\boldsymbol{\theta}}[\mathbf{FIM}(\mathbf{y}; \boldsymbol{\lambda})] = \mathbf{FIM}(\mathbf{y}; \boldsymbol{\lambda}). \quad (31)$$

### B. Derivation of $\mathbb{E}_{\boldsymbol{\theta}} \left[ -\frac{\partial}{\partial \boldsymbol{\lambda}} \left( \frac{\partial \log p(\boldsymbol{\theta})}{\partial \boldsymbol{\lambda}} \right)^\top \right]$

Since  $\boldsymbol{\theta} \sim \mathcal{N}(\mathbf{0}_{N \times 1}, \boldsymbol{\Psi})$ , we can calculate  $\log p(\boldsymbol{\theta})$  by  $\log p(\boldsymbol{\theta}) = -\frac{1}{2} \boldsymbol{\theta}^\top \boldsymbol{\Psi}^{-1} \boldsymbol{\theta} - \frac{N}{2} \log(2\pi) - \frac{1}{2} \log \det \boldsymbol{\Psi}$ , and its partial to  $\boldsymbol{\lambda}$  can be calculated by

$$\frac{\partial \log p(\boldsymbol{\theta})}{\partial \boldsymbol{\lambda}} = [0, -(\boldsymbol{\Psi}^{-1} \boldsymbol{\theta})^\top, 0, 0, 0]^\top. \quad (32)$$

Subsequently,  $\mathbb{E}_{\boldsymbol{\theta}} \left[ -\frac{\partial}{\partial \boldsymbol{\lambda}} \left( \frac{\partial \log p(\boldsymbol{\theta})}{\partial \boldsymbol{\lambda}} \right)^\top \right]$  can be expressed by

$$\begin{aligned} \mathbb{E}_{\boldsymbol{\theta}} \left[ -\frac{\partial}{\partial \boldsymbol{\lambda}} \left( \frac{\partial \log p(\boldsymbol{\theta})}{\partial \boldsymbol{\lambda}} \right)^\top \right] &= -\frac{\partial}{\partial \boldsymbol{\lambda}} \left( \frac{\partial \log p(\boldsymbol{\theta})}{\partial \boldsymbol{\lambda}} \right)^\top \\ &= \text{Blkdiag}(0, \boldsymbol{\Psi}^{-1}, \mathbf{0}_{3 \times 3}). \end{aligned} \quad (33)$$

### C. Derivation of the Transformed HCRLB

Due to the ambiguity between the parameters to be estimated, the MSE of CFO and PN is jointly calculated using (26), and when computing the *position error bound* (PEB), the position parameters are required to be in the form of 3D Cartesian coordinates  $x_u$ ,  $y_u$ , and  $z_u$ . Therefore, the parameter vector  $\boldsymbol{\lambda}$  needs to be transformed into  $\boldsymbol{\alpha}$ . The HCRLB for  $\boldsymbol{\alpha}$  is given by [9]

$$\mathbf{HCRLB}(\mathbf{p}_u, \mathbf{w}) = \boldsymbol{\Xi}(\mathbf{p}_u) \mathbf{B}^{-1}(\mathbf{p}_u, \mathbf{w}) \boldsymbol{\Xi}^\top(\mathbf{p}_u), \quad (34)$$

where for any UE position  $\mathbf{p}_u$ ,  $\boldsymbol{\Xi}(\mathbf{p}_u)$  is the transition matrix defined as

$$\boldsymbol{\Xi}(\mathbf{p}_u) = \frac{\partial \mathbf{g}(\boldsymbol{\lambda})}{\partial \boldsymbol{\lambda}} = \text{Blkdiag}(\boldsymbol{\Xi}_1, \boldsymbol{\Xi}_2(\mathbf{p}_u)), \quad (35)$$

and  $\boldsymbol{\Xi}_1$ ,  $\boldsymbol{\Xi}_2(\mathbf{p}_u)$  can be calculated by (36) and (37).

After obtaining  $\mathbf{HCRLB}(\mathbf{p}_u, \mathbf{w})$ , PEB for position estimation and  $\mathbf{HCRLB}_{\text{CFO-PN}}$  for CFO-PN estimation can be calculated as

$$\text{PEB} = \sqrt{\text{tr}([\mathbf{HCRLB}(\mathbf{p}_u, \mathbf{w})]_{N:N+2, N:N+2})}, \quad (38)$$

$$\mathbf{HCRLB}_{\text{CFO-PN}} = \text{tr}([\mathbf{HCRLB}(\mathbf{p}_u, \mathbf{w})]_{0:N-1, 0:N-1}). \quad (39)$$

Both PEB and  $\mathbf{HCRLB}_{\text{CFO-PN}}$  are related to UE's location  $\mathbf{p}_u$  and RIS phase shift  $\mathbf{w}$ .

### V. RIS PHASE SHIFT OPTIMIZATION

In this section, our goal is to optimize the phase shift of the RIS to enhance theoretical positioning accuracy, i.e., PEB. According to equation (38), minimizing the PEB at a specific location requires knowledge of that location. However, this is not possible in practical positioning scenarios. To address this issue, we select multiple sampling points within the AOI randomly, then calculate and minimize their average PEB. Accordingly, the optimization problem for RIS phase shift can be expressed as

$$\begin{aligned} \min_{\mathbf{w}} \quad & \frac{1}{U} \sum_{u=1}^U \text{PEB}(\mathbf{p}_u, \mathbf{w}) \\ \text{s.t.} \quad & |\mathbf{w}[r]| = 1, r = 1, \dots, N_R. \end{aligned} \quad (40)$$

Problem (40) is non-convex because the objective function does not exhibit convexity with respect to vector  $\mathbf{w}$ . We define  $\mathbf{W} \triangleq \bar{\mathbf{w}} \bar{\mathbf{w}}^\top$ , where  $\bar{\mathbf{w}} \triangleq \mathbf{w}^*$ , which needs to satisfy  $\mathbf{W} \succeq 0$  and  $\text{rank}(\mathbf{W}) = 1$ . Since the rank-1 constraint is non-convex, we employ the SDR method to relax this constraint. Consequently, the problem (40) can be transformed into

$$\begin{aligned} \min_{\mathbf{W}} \quad & \frac{1}{U} \sum_{u=1}^U \text{PEB}(\mathbf{p}_u, \mathbf{W}) \\ \text{s.t.} \quad & [\mathbf{W}]_{r,r} = 1, r = 1, \dots, N_R, \\ & \mathbf{W} \succeq 0. \end{aligned} \quad (41)$$

Inspired by [12], we utilize the property of the Schur complement [6], and the problem can be expressed in the form of SDP. For each calculated PEB at a particular position  $\mathbf{p}_u$ , we define an auxiliary matrix  $\mathbf{Z}_u$  that satisfies the following expression

$$\mathbf{Z}_u \succeq \tilde{\boldsymbol{\Xi}}(\mathbf{p}_u) \mathbf{B}^{-1}(\mathbf{p}_u, \mathbf{W}) \tilde{\boldsymbol{\Xi}}^\top(\mathbf{p}_u), \quad (42)$$

where  $\tilde{\boldsymbol{\Xi}}(\mathbf{p}_u) \triangleq \mathbf{T} \boldsymbol{\Xi}(\mathbf{p}_u)$ , and  $\mathbf{T} \triangleq [\mathbf{0}_{N \times N} \ \mathbf{I}_3] \in \mathbb{R}^{(N+3) \times (N+3)}$  can extract the PEB portion from the HCRLB.

$$\Xi_1 = \begin{bmatrix} \frac{\partial \gamma[0]}{\partial \phi} & \frac{\partial \gamma[0]}{\partial \theta[0]} & \cdots & \frac{\partial \gamma[0]}{\partial \theta[N-1]} \\ \vdots & \vdots & \ddots & \vdots \\ \frac{\partial \gamma[N-1]}{\partial \phi} & \frac{\partial \gamma[N-1]}{\partial \theta[0]} & \cdots & \frac{\partial \gamma[N-1]}{\partial \theta[N-1]} \end{bmatrix} = \begin{bmatrix} 0 & 0 & 0 & \cdots & 0 \\ \frac{2\pi}{N} & -1 & 1 & \cdots & 0 \\ \vdots & \vdots & \ddots & \ddots & \vdots \\ \frac{2\pi(N-1)}{N} & -1 & 0 & \cdots & 1 \end{bmatrix} \in \mathbb{R}^{N \times (N+1)}, \quad (36)$$

$$\Xi_2(\mathbf{p}_u) = \begin{bmatrix} \frac{\partial x_u}{\partial d_{Ru}} & \frac{\partial x_u}{\partial \phi_{az}} & \frac{\partial x_u}{\partial \phi_{el}} \\ \frac{\partial y_u}{\partial d_{Ru}} & \frac{\partial y_u}{\partial \phi_{az}} & \frac{\partial y_u}{\partial \phi_{el}} \\ \frac{\partial z_u}{\partial d_{Ru}} & \frac{\partial z_u}{\partial \phi_{az}} & \frac{\partial z_u}{\partial \phi_{el}} \end{bmatrix} = \begin{bmatrix} \sin \phi_{el} \cos \phi_{az} & -d_{Ru} \sin \phi_{el} \sin \phi_{az} & d_{Ru} \cos \phi_{az} \cos \phi_{el} \\ \sin \phi_{el} \sin \phi_{az} & d_{Ru} \sin \phi_{el} \cos \phi_{az} & d_{Ru} \sin \phi_{az} \cos \phi_{el} \\ \cos \phi_{el} & 0 & -d_{Ru} \sin \phi_{el} \end{bmatrix} \in \mathbb{R}^{3 \times 3}. \quad (37)$$

The optimization problem in (40) can be converted to

$$\begin{aligned} \min_{\mathbf{W}, \mathbf{Z}_1, \dots, \mathbf{Z}_U} \quad & \frac{1}{U} \sum_{u=1}^U \text{tr}(\mathbf{Z}_u) \\ \text{s.t.} \quad & [\mathbf{W}]_{r,r} = 1, r = 1, \dots, N_R, \\ & \mathbf{W} \succcurlyeq 0, \\ & \frac{1}{U} \sum_{u=1}^U \begin{bmatrix} \mathbf{Z}_u & \tilde{\Xi}(\mathbf{p}_u) \\ \tilde{\Xi}^\top(\mathbf{p}_u) & \mathbf{B}(\mathbf{p}_u, \mathbf{W}) \end{bmatrix} \succcurlyeq 0. \end{aligned} \quad (43)$$

Problem (43) is a convex SDP problem, and can be optimally solved using established convex optimization solvers, such as CVX [30]. Since there is no rank-1 constraint in the optimization problem, it is highly likely that the obtained matrix  $\mathbf{W}$  will have a rank greater than one. Therefore, decomposing it into the desired RIS phase shift vector  $\mathbf{w}$  is a crucial subsequent problem. As in [29], we first perform an eigenvalue decomposition on the optimal  $\mathbf{W}$ , then take the largest eigenvector and multiply it by the square root of the largest eigenvalue and normalize the vector, obtaining  $\bar{\mathbf{w}}$ . Finally, we calculate the RIS phase shift by  $\mathbf{w} = \bar{\mathbf{w}}^*$ . The decomposition process can also be accomplished using the Gaussian randomization method as in [28].

In order to meet the requirements of (43), we next derive the expression of  $\mathbf{B}$  that is related to  $\mathbf{W}$ . We first rewrite (4) as

$$\mathbf{y} = \sqrt{P} \mathbf{\Lambda}_\phi \mathbf{\Lambda}_\theta \mathbf{S}^\top \mathbf{G}^\top \mathbf{w} + \mathbf{v}, \quad (44)$$

which separates  $\mathbf{w}$  from  $\mathbf{h}$ , with  $\mathbf{G} \in \mathbb{C}^{N_R \times N}$  and  $[\mathbf{G}]_{r,n} = \sqrt{\rho_{aR,n,r}} \sqrt{\rho_{Ru,n,r}} e^{-j2\pi \frac{nB}{N}(\tau_{ar} + \tau_{ru})}$ .

Correspondingly,  $\boldsymbol{\mu}$  can be rewritten as  $\boldsymbol{\mu} = \sqrt{P} \mathbf{\Lambda}_\phi \mathbf{\Lambda}_\theta \mathbf{S}^\top \mathbf{G}^\top \bar{\mathbf{w}}^*$ . Furthermore, we can express each term of  $\boldsymbol{\mu}$  and its conjugate as

$$\begin{aligned} \boldsymbol{\mu}[n] = \boldsymbol{\mu}[n]^\top &= \sqrt{P} e^{j(\theta[n] + 2\pi \frac{n}{N} \phi)} [\mathbf{S}^\top]_{:,n} \mathbf{G}^\top \bar{\mathbf{w}}^* \\ &= \sqrt{P} e^{j(\theta[n] + 2\pi \frac{n}{N} \phi)} \bar{\mathbf{w}}^\text{H} \mathbf{G} [\mathbf{S}]_{:,n}, \end{aligned} \quad (45)$$

and

$$\boldsymbol{\mu}[n]^* = \sqrt{P} e^{-j(\theta[n] + 2\pi \frac{n}{N} \phi)} [\mathbf{S}]_{:,n}^\text{H} \mathbf{G}^\text{H} \bar{\mathbf{w}}. \quad (46)$$

According to (28), only the  $\mathbf{FIM}(\mathbf{y}; \boldsymbol{\lambda})$  part is related to  $\mathbf{w}$ , hence we only need to derive the relationship of this part of  $\mathbf{B}$  and  $\mathbf{W}$ . We can rewrite the  $\mathbf{FIM}$  in a summation form:

$$[\mathbf{FIM}(\mathbf{y}; \boldsymbol{\lambda})]_{i,j} = \frac{2}{\sigma^2} \sum_{n=0}^{N-1} \Re \left\{ \frac{\partial \boldsymbol{\mu}[n]^*}{\partial \lambda_i} \frac{\partial \boldsymbol{\mu}[n]}{\partial \lambda_j} \right\}. \quad (47)$$

The partial derivatives of  $\boldsymbol{\mu}[n]$  and  $\boldsymbol{\mu}[n]^*$  with respect to all parameters to be estimated are derived in Appendix A. It is

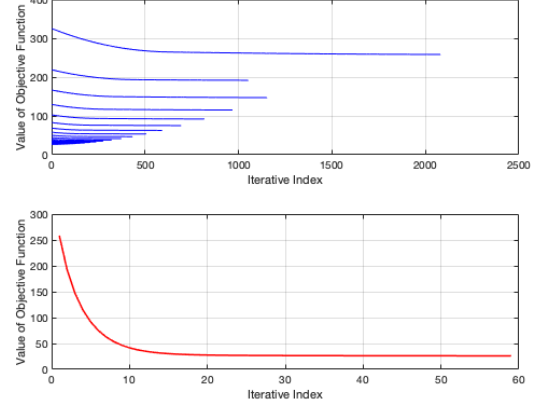


Fig. 3. The convergence of Algorithm 1.

observed that the expressions for  $\frac{\partial \boldsymbol{\mu}[n]^*}{\partial \lambda_i}$  all end with  $\bar{\mathbf{w}}$ , while the expressions for  $\frac{\partial \boldsymbol{\mu}[n]}{\partial \lambda_j}$  all start with  $\bar{\mathbf{w}}^\text{H}$  for the vector parts. Therefore, when calculating the  $\mathbf{FIM}$ , we can easily obtain the expression with respect to  $\mathbf{W}$ .

## VI. NUMERICAL RESULTS

This section presents comprehensive simulations conducted to assess the performance of the proposed estimation and optimization algorithms. We consider a 3D Cartesian coordinate system, where the AN is located at  $\mathbf{p}_a = [2\text{m}, -2\text{m}, 1\text{m}]^\top$ , and the reference point of RIS is located at  $\mathbf{0}_{3 \times 1}$ . Without loss of generality, RIS is placed on the  $yz$  plane. We assume AOI in a cube centered at  $[2\text{m}, 2\text{m}, 0\text{m}]^\top$  with the edge length of 1m. We set light speed  $c = 3 \times 10^8 \text{m/s}$ , noise power  $\sigma^2 = -109 \text{dBm}$ .  $N = 32$  subcarriers are used in one OFDM symbol, and the central frequency and bandwidth of the OFDM symbol are set to  $f_c = 2.8 \text{GHz}$  and  $B = 100 \text{MHz}$ , respectively. The normalized CFO  $\phi$  is uniformly drawn from  $[-0.15, 0.15]$ , and the length of shortened PN vector  $L$  is set as  $L = 16$ . Additionally, we make the assumption that the antenna gains,  $G_a$  and  $G_t$ , are equal to 1.

### A. Convergence analysis

To begin, we analyze the convergence of the proposed joint estimation algorithm. Fig. 3 illustrates the convergence of the algorithm in the case of transmit power of  $-10 \text{dBm}$ , which corresponds to a receiving *signal-to-noise ratio* (SNR)

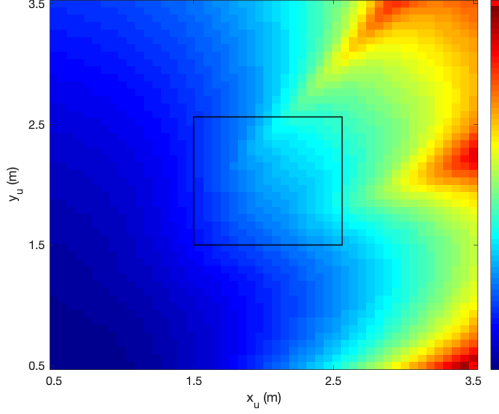


Fig. 4. Apply random RIS phase shift and calculate the PEB of different positions.

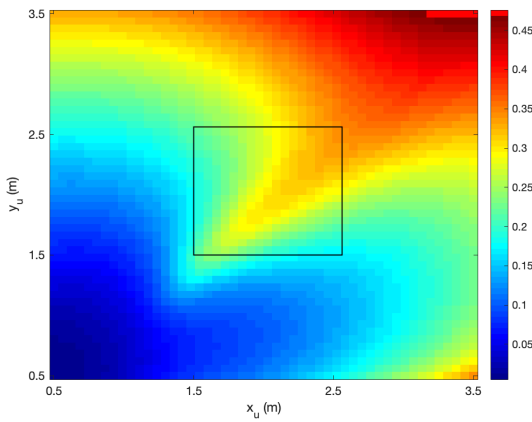


Fig. 5. Apply the RIS phase shift optimization algorithm and calculate the PEB of different positions.

of approximately 17.5dB. Specifically, Fig. 3 (a) shows the variation of the objective function during each inner GD iteration in Algorithm 1, while Fig. 3 (b) focuses solely on the variation of the objective function based on the results after every inner iteration. From Fig. 3 (a), we observe that the inner GD iterations corresponding to each outer iteration converge earlier and earlier. This phenomenon occurs because the convergence for outer iteration approaches, the magnitude of the parameter updates decreases, and the variation of the posterior function becomes closer to the predefined stopping threshold. From Fig. 3, it is not difficult to notice that the inner loop typically converges within 2000 iterations, while the outer loop generally converges within 40 iterations.

#### B. Performance of RIS Phase Shift Optimization

In this subsection, our attention is directed toward evaluating the performance of the optimization algorithm. Fig. 4 and Fig. 5 illustrate the PEB near the AOI before and after the optimization of RIS phase shift, respectively. More precisely, we configure the number of RIS elements, denoted as  $N_R$ , to be 81, and transmit power  $P$  to be  $-20$ dBm, which corresponds

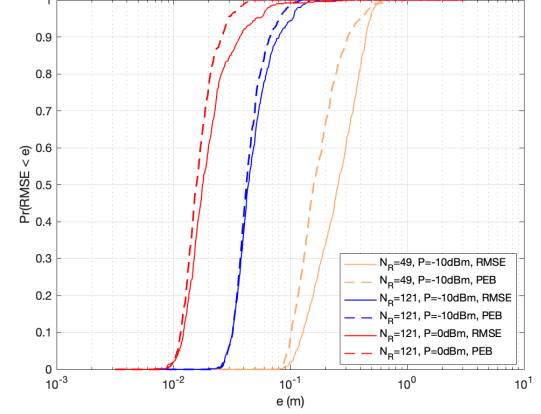


Fig. 6. The CDF of RMSE and PEB with different  $N_R$  and transmit powers.

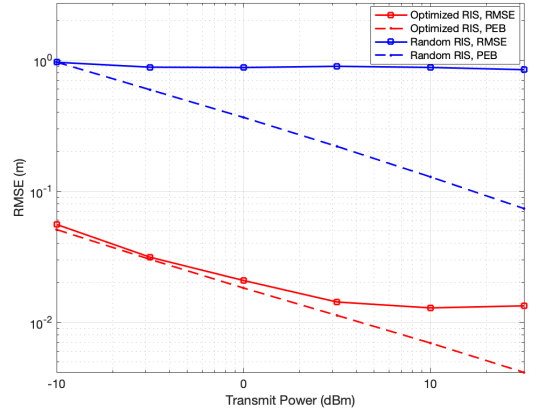


Fig. 7. The RMSE of  $p_u$  estimation with random and optimized RIS phase shift.

to a receiving SNR of approximately 7.5dB. Without loss of generality, the selected positions in the figures are located in the  $xy$  plane. A comparison between the two figures reveals that the optimized PEB has improved by approximately two orders of magnitude, which fully demonstrates the effectiveness of the employed RIS optimization algorithm. Additionally, we have observed that the optimized RIS phase shift not only improves the theoretical positioning accuracy within the AOI, but also has a significant improvement in the surrounding areas of it.

#### C. Localization Accuracy

In this subsection, we first illustrate the overall positioning accuracy. Fig. 6 presents the *cumulative distribution functions* (CDFs) of RMSE and PEB for 500 random testing positions, under different transmit powers and the number of RIS elements. It can be observed that increasing the RIS size and the transmit power both lead to an improvement in the overall positioning accuracy. Furthermore, we find that when the RIS size is set to  $N_R = 49$ , the CDF of RMSE deviates significantly from the CDF of PEB, and doesn't achieve the theoretical positioning accuracy. However, when the RIS size

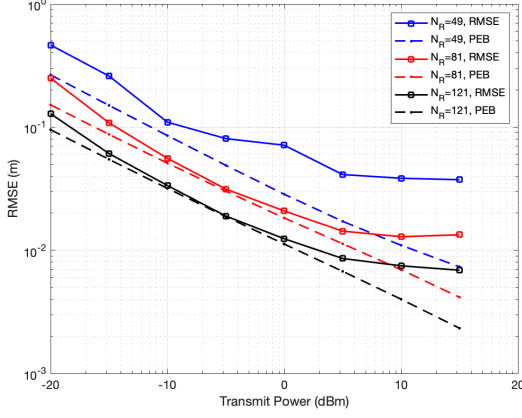


Fig. 8. The RMSE of  $\mathbf{p}_u$  estimation at  $N_R = 49$ ,  $N_R = 81$ , and  $N_R = 121$ .

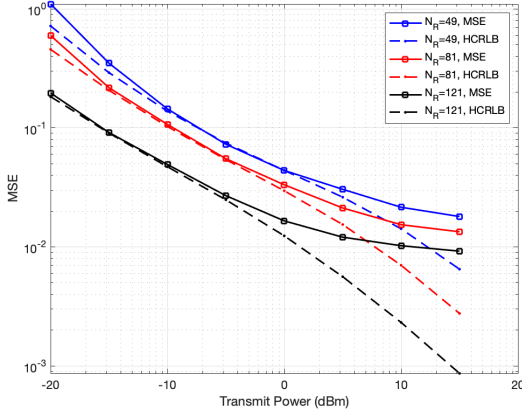


Fig. 9.  $MSE_{\phi, \theta}$  at  $N_R = 49$ ,  $N_R = 81$ , and  $N_R = 121$ .

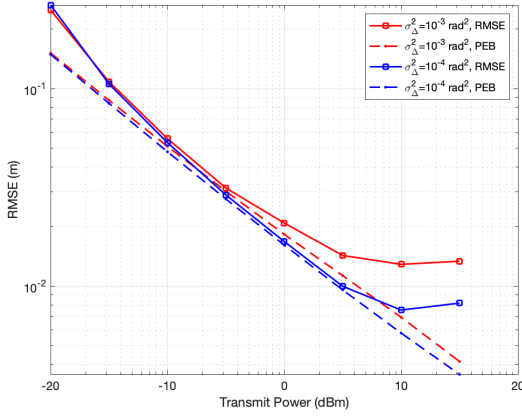


Fig. 10.  $RMSE_u$  at  $\sigma_{\Delta}^2 = 10^{-3} \text{ rad}^2$  and  $\sigma_{\Delta}^2 = 10^{-4} \text{ rad}^2$ .

is increased to  $N_R = 121$ , the CDF of the RMSE curve aligns more closely with the CDF of PEB. This phenomenon can also be observed in Fig. 8.

Next, we select a fixed testing position at coordinate  $[1.50\text{m}, 2.15\text{m}, 0.45\text{m}]^\top$  (rounded to two decimal places for convenience) to investigate the impact of transmit power  $P$ ,

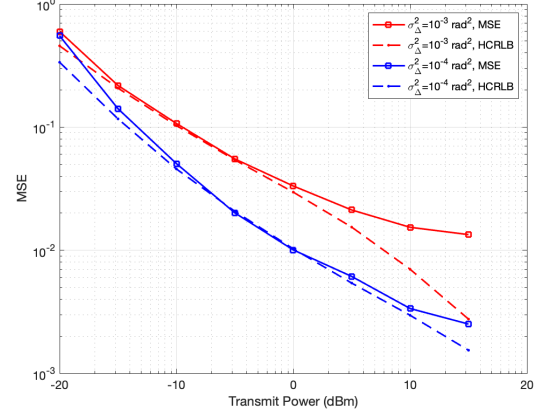


Fig. 11.  $MSE_{\phi, \theta}$  at  $\sigma_{\Delta}^2 = 10^{-3} \text{ rad}^2$  and  $\sigma_{\Delta}^2 = 10^{-4} \text{ rad}^2$ .

RIS size  $N_R$ , and PN variance  $\sigma_{\Delta}^2$  on the estimation accuracy of UE position, CFO, and PN.

In Fig. 7, we fix the number of RIS elements at 81 and assess the impact of random RIS phase shift versus optimized RIS configuration on positioning accuracy. It is evident that the actual positioning performance with random RIS phase shift does not experience a significant decline as the transmit power increases. At the other extreme, the optimized RIS phase shift provides an improvement of approximately two orders of magnitude in positioning accuracy. This fully demonstrates the crucial role of optimizing the RIS phase shift in localization problems and the effectiveness of the optimization method we employed.

Fig. 8 and Fig. 9 respectively depict the curves of RMSE for positioning and MSE for estimation of  $\gamma$  under different transmit powers, at the number of RIS sizes of 49, 81, and 121. It can be observed that increasing the transmit power and the number of RIS elements results in gains in all parameters to be estimated. This demonstrates that increasing the signal transmit power or increasing the number of RIS reflection elements is beneficial for parameter estimation.

Fig. 10 and Fig. 11 respectively illustrate the RMSE for positioning and MSE for estimation of  $\gamma$  when  $N_R$  is set to 81, with PN variances  $\sigma_{\Delta}^2 = 10^{-3} \text{ rad}^2$  and  $\sigma_{\Delta}^2 = 10^{-4} \text{ rad}^2$ . The results demonstrate that decreasing the PN covariance leads to significant improvements in combined estimation performance.

## VII. CONCLUSION

This paper investigates the optimization of RIS phase shift and the joint estimation of CFO, PN, and UE position under imperfect channel conditions for an OFDM system in a near-field static localization scenario. An iterative joint estimation algorithm based on the MAP criterion and GD algorithm is proposed. Extensive simulation results have demonstrated that by optimizing the RIS phase shift, the theoretical positioning accuracy has been improved by two orders of magnitude. Moreover, the maximum positioning accuracy can be lower than  $10^{-2} \text{ m}$ . These findings strongly support the efficacy of the proposed estimation and optimization algorithms in the

paper. In order to further improve the estimation performance and support a larger AOI, the optimization algorithm used in this paper requires averaging a large number of PEBs related to random positions and will result in extremely high computation complexity. Hence, it becomes imperative to utilize an optimization algorithm with reduced complexity in this scenario. This would be a fruitful area for further work.

## APPENDIX A

### DERIVATION OF PARTIAL DERIVATIVES OF $\mu[n]$ AND $\mu[n]^*$

The partial derivatives of  $\mu[n]$  with respect to all parameters to be estimated are derived as follows

$$\frac{\partial \mu[n]}{\partial \phi} = \sqrt{P} \frac{2\pi n}{N} e^{j(\theta[n]+2\pi \frac{n}{N}\phi)} \bar{w}^H \mathbf{G}[\mathbf{S}]_{:,n}, \quad (48a)$$

$$\frac{\partial \mu[n]}{\partial \theta[n]} = \sqrt{P} e^{j(\theta[n]+2\pi \frac{n}{N}\phi)} \bar{w}^H \mathbf{G}[\mathbf{S}]_{:,n}, \quad (48b)$$

$$\frac{\partial \mu[n]}{\partial \theta[m]} = 0, m \neq n, \quad (48c)$$

$$\frac{\partial \mu[n]}{\partial d_{Ru}} = \sqrt{P} e^{j(\theta[n]+2\pi \frac{n}{N}\phi)} \bar{w}^H \frac{\partial \mathbf{G}}{\partial d_{Ru}} [\mathbf{S}]_{:,n}, \quad (48d)$$

$$\frac{\partial \mu[n]}{\partial \phi_{az}} = \sqrt{P} e^{j(\theta[n]+2\pi \frac{n}{N}\phi)} \bar{w}^H \frac{\partial \mathbf{G}}{\partial \phi_{az}} [\mathbf{S}]_{:,n}, \quad (48e)$$

$$\frac{\partial \mu[n]}{\partial \phi_{el}} = \sqrt{P} e^{j(\theta[n]+2\pi \frac{n}{N}\phi)} \bar{w}^H \frac{\partial \mathbf{G}}{\partial \phi_{el}} [\mathbf{S}]_{:,n}, \quad (48f)$$

and the partial derivatives of  $\mu[n]^*$  with respect to all parameters to be estimated are derived as follows

$$\frac{\partial \mu[n]^*}{\partial \phi} = -j \sqrt{P} \frac{2\pi n}{N} e^{-j(\theta[n]+2\pi \frac{n}{N}\phi)} [\mathbf{S}]_{:,n}^H \mathbf{G}^H \bar{w}, \quad (49a)$$

$$\frac{\partial \mu[n]^*}{\partial \theta[n]} = -j \sqrt{P} e^{-j(\theta[n]+2\pi \frac{n}{N}\phi)} [\mathbf{S}]_{:,n}^H \mathbf{G}^H \bar{w}, \quad (49b)$$

$$\frac{\partial \mu[n]^*}{\partial \theta[m]} = 0, m \neq n, \quad (49c)$$

$$\frac{\partial \mu[n]^*}{\partial d_{Ru}} = \sqrt{P} e^{-j(\theta[n]+2\pi \frac{n}{N}\phi)} [\mathbf{S}]_{:,n}^H \left( \frac{\partial \mathbf{G}}{\partial d_{Ru}} \right)^H \bar{w}, \quad (49d)$$

$$\frac{\partial \mu[n]^*}{\partial \phi_{az}} = \sqrt{P} e^{-j(\theta[n]+2\pi \frac{n}{N}\phi)} [\mathbf{S}]_{:,n}^H \left( \frac{\partial \mathbf{G}}{\partial \phi_{az}} \right)^H \bar{w}, \quad (49e)$$

$$\frac{\partial \mu[n]^*}{\partial \phi_{el}} = \sqrt{P} e^{-j(\theta[n]+2\pi \frac{n}{N}\phi)} [\mathbf{S}]_{:,n}^H \left( \frac{\partial \mathbf{G}}{\partial \phi_{el}} \right)^H \bar{w}. \quad (49f)$$

## REFERENCES

- [1] A. Bourdoux, A. N. Barreto, van Liempd *et al.*, “6G white paper on localization and sensing,” *arXiv preprint arXiv:2006.01779*, 2020.
- [2] S. Dang, O. Amin, B. Shihada *et al.*, “What should 6G be?” *Nature Electronics*, vol. 3, no. 1, pp. 20–29, 2020.
- [3] K. B. Letaief, W. Chen, Y. Shi *et al.*, “The roadmap to 6G: AI empowered wireless networks,” *IEEE communications magazine*, vol. 57, no. 8, pp. 84–90, 2019.
- [4] Q. Wu, S. Zhang, B. Zheng *et al.*, “Intelligent reflecting surface-aided wireless communications: A tutorial,” *IEEE Transactions on Communications*, vol. 69, no. 5, pp. 3313–3351, 2021.
- [5] X. Yuan, Y.-J. A. Zhang, Y. Shi *et al.*, “Reconfigurable-intelligent-surface empowered wireless communications: Challenges and opportunities,” *IEEE wireless communications*, vol. 28, no. 2, pp. 136–143, 2021.
- [6] S. P. Boyd and L. Vandenberghe, *Convex optimization*. Cambridge university press, 2004.
- [7] H. L. Van Trees, *Detection, estimation, and modulation theory. part I: detection, estimation, and linear modulation theory*. John Wiley & Sons, 2004.
- [8] C. A. Balanis, *Antenna theory: analysis and design*. John Wiley & Sons, 2016.
- [9] S. M. Kay, *Fundamentals of statistical signal processing: estimation theory*. Prentice-Hall, Inc., 1993.
- [10] A. Shahmansoori, G. E. Garcia, G. Destino *et al.*, “Position and orientation estimation through millimeter-wave MIMO in 5G systems,” *IEEE Transactions on Wireless Communications*, vol. 17, no. 3, pp. 1822–1835, 2017.
- [11] A. Hu, T. Lv, H. Gao *et al.*, “An ESPRIT-based approach for 2-D localization of incoherently distributed sources in massive MIMO systems,” *IEEE Journal of Selected Topics in Signal Processing*, vol. 8, no. 5, pp. 996–1011, 2014.
- [12] M. Luan, B. Wang, Y. Zhao *et al.*, “Phase design and near-field target localization for RIS-assisted regional localization system,” *IEEE Transactions on Vehicular Technology*, vol. 71, no. 2, pp. 1766–1777, 2021.
- [13] A. Elzanaty, A. Guerra, F. Guidi *et al.*, “Reconfigurable intelligent surfaces for localization: Position and orientation error bounds,” *IEEE Transactions on Signal Processing*, vol. 69, pp. 5386–5402, 2021.
- [14] Y. Lin, S. Jin, M. Matthaiou *et al.*, “Channel estimation and user localization for IRS-assisted MIMO-OFDM systems,” *IEEE Transactions on Wireless Communications*, vol. 21, no. 4, pp. 2320–2335, 2021.
- [15] B. Teng, X. Yuan, R. Wang *et al.*, “Bayesian user localization and tracking for reconfigurable intelligent surface aided MIMO systems,” *IEEE Journal of Selected Topics in Signal Processing*, vol. 16, no. 5, pp. 1040–1054, 2022.
- [16] D. Dardari, N. DeCarli, A. Guerra *et al.*, “LOS/NLOS near-field localization with a large reconfigurable intelligent surface,” *IEEE Transactions on Wireless Communications*, vol. 21, no. 6, pp. 4282–4294, 2021.
- [17] R. Ghazalian, K. Keykhoosravi, H. Chen *et al.*, “Bi-static sensing for near-field RIS localization,” in *GLOBECOM 2022-2022 IEEE Global Communications Conference*. IEEE, 2022, pp. 6457–6462.
- [18] Y. Han, S. Jin, C.-K. Wen *et al.*, “Localization and channel reconstruction for extra large RIS-assisted massive MIMO systems,” *IEEE Journal of Selected Topics in Signal Processing*, vol. 16, no. 5, pp. 1011–1025, 2022.
- [19] Z. Wang, Z. Liu, Y. Shen *et al.*, “Location awareness in beyond 5G networks via reconfigurable intelligent surfaces,” *IEEE Journal on Selected Areas in Communications*, vol. 40, no. 7, pp. 2011–2025, 2022.
- [20] K. Keykhoosravi, M. F. Keskin, S. Dwivedi *et al.*, “Semi-passive 3D positioning of multiple RIS-enabled users,” *IEEE Transactions on Vehicular Technology*, vol. 70, no. 10, pp. 11 073–11 077, 2021.
- [21] D. D. Lin and T. J. Lim, “The variational inference approach to joint data detection and phase noise estimation in OFDM,” *IEEE Transactions on Signal Processing*, vol. 55, no. 5, pp. 1862–1874, 2007.
- [22] D. D. Lin, R. A. Pacheco, T. J. Lim *et al.*, “Joint estimation of channel response, frequency offset, and phase noise in OFDM,” *IEEE Transactions on Signal Processing*, vol. 54, no. 9, pp. 3542–3554, 2006.
- [23] M. A. ElMossallamy, H. Zhang, L. Song *et al.*, “Reconfigurable intelligent surfaces for wireless communications: Principles, challenges, and opportunities,” *IEEE Transactions on Cognitive Communications and Networking*, vol. 6, no. 3, pp. 990–1002, 2020.
- [24] X. Zhang and H. Zhang, “Hybrid reconfigurable intelligent surfaces-assisted near-field localization,” *IEEE Communications Letters*, vol. 27, no. 1, pp. 135–139, 2022.
- [25] E. D. Kaplan and C. Hegarty, *Understanding GPS/GNSS: principles and applications*. Artech house, 2017.
- [26] N. Zhu, J. Marais, D. Bétaillé *et al.*, “GNSS position integrity in urban environments: A review of literature,” *IEEE Transactions on Intelligent Transportation Systems*, vol. 19, no. 9, pp. 2762–2778, 2018.
- [27] O. Montenbruck, P. Steigenberger, L. Prange *et al.*, “The multi-GNSS experiment (MGEX) of the international GNSS service (IGS)–achievements, prospects and challenges,” *Advances in space research*, vol. 59, no. 7, pp. 1671–1697, 2017.
- [28] Q. Wu and R. Zhang, “Intelligent reflecting surface enhanced wireless network: Joint active and passive beamforming design,” in *2018 IEEE Global Communications Conference (GLOBECOM)*. IEEE, 2018, pp. 1–6.
- [29] X. Yu, J.-C. Shen, J. Zhang *et al.*, “Alternating minimization algorithms for hybrid precoding in millimeter wave MIMO systems,” *IEEE Journal of Selected Topics in Signal Processing*, vol. 10, no. 3, pp. 485–500, 2016.
- [30] M. Grant and S. Boyd, “CVX: Matlab software for disciplined convex programming, version 2.1,” 2014.
- [31] Y. Liu, E. Liu, R. Wang *et al.*, “Reconfigurable intelligent surface aided wireless localization,” in *ICC 2021-IEEE International Conference on Communications*. IEEE, 2021, pp. 1–6.

[32] R. Wang, Z. Xing, E. Liu *et al.*, “Joint localization and communication study for intelligent reflecting surface aided wireless communication system,” *IEEE Transactions on Communications*, 2023.